Jets in bubbles

A. PEARSON, J.R. BLAKE and S.R. OTTO
*School of Mathematics and Statistics, The University of Birmingham, Edgbaston, Birmingham B15 2TT,
United Kingdom (e-mails: A.Pearson@bham.ac.uk; J.R.Blake@bham.ac.uk; S.R.Otto@bham.ac.uk)*

Abstract. Different types of jet formation in collapsing cavitation and gas bubbles near a rigid boundary are explored by using an advanced boundary-integral technique which incorporates the transition from simply connected to multiply connected bubbles (*i.e.* toroidal bubbles). Physical interpretation and understanding is facilitated by the calculation of the evolving bubble shape, fluid velocities and pressures, the partitioning of kinetic, potential and gravitational energies, the circulation around the bubble and the Kelvin impulse associated with both the complete bubble and the high-speed liquid jet. In the most vigorous jet formation examples considered it is found that upto 31% of the total energy and upto 53% of the Kelvin impulse is associated with the jet. Practical implications of this study beyond the usual damage mechanisms imply that the level of bubble compression will be signiffcantly lessened leading to lower bubble gas temperatures and thence the corresponding change in the chemical reactivity of its contents or the emission of light. Calculations also suggest interesting phenomena around a standoff distance of 1·2 maximum bubble radii where the circulation around the bubble and the kinetic energy of the jet appear to have maximum values. The practical implications and experimental confirmation of this are yet to be explored.

Key words: bubble, cavitation, circulation, Kelvin impulse, liquid jet, toroidal

1. An overview

Over the past few decades, several computational techniques have been employed to calculate the motion of bubbles, cavities and drops for a wide range of physical problems. Many of the more violent or rapid motions may be effectively reduced to inviscid potential problems which are valid for much of the lifetime of the respective bodies: thus requiring solution of Laplace's equation in the fluid domain. In the current work, we choose to use a direct boundary-integral method based on Green's identity, which allows us to formulate the problem entirely on the boundaries of the fluid domain, effectively reducing the number of dimensions of the problem by one.

In ascertaining the motion of bubbles in close proximity to boundaries, the consideration of non-spherical effects is paramount in obtaining an understanding of the physical problem. However, further from the boundary spherical bubble models have been shown to be a good indicator of gross behaviour having been employed since the inception of work in this field by Rayleigh [1]. Although we are now fully aware of the non-spherical behaviour of bubbles in many physical situations, the assumption of a spherical bubble allows researchers to readily introduce the consideration of many physical phenomena into a simple equation of motion. Historically these include effects due to: the presence of nearby boundaries [2], surface tension and viscosity, or weakly compressible effects [3, 4]. More recently, aspects such as the introduction of heat and mass transfer effects were considered [5, 6]. Such models are mentioned as many of the effects may be included (albeit in some cases with a high degree of difficulty) within boundary-integral schemes (*e.g.* heat and mass transfer [7]).

The first application of the boundary-integral method to the field of bubble dynamics may be attributed to Lenoir [8] who considers the collapse of an initially spherical bubble near to both rigid and free boundaries. A more successful consideration of the collapse of a spherical void near a rigid boundary may be found in the conference paper by [9], though the necessary brevity of the paper limits the number of cases considered. The main drawback to these early studies is that the bubble is assumed to collapse from an initially spherical maximum volume, and as such, no consideration is given to the expansion phase of the bubble. Despite the proven, stable nature of the expansion phase [10] it is essential to calculate the expansion phase of the bubble where any source of asymmetry is present in the flow domain, since any perturbation from a spherical state during expansion may have great influence during the unstable collapse phase. This reasoning holds true even for bubbles formed several maximum radii from the boundary where bubble-surface geometry may appear spherical, yet is often not, with further non-spherical attributes becoming apparent if consideration is given to surface velocities or quantities in the surrounding fluid.

The first study which considers both the growth and collapse of a bubble may be attributed to Taib [11]. In this work, the bubble is assumed to grow from a small, initially spherical shape upto maximum volume, following which, collapse ensues and the motion is followed (in most cases) through to the time of liquid-jet impact. Despite the primitive piecewise-linear representation of the surface geometry and potential used in this work and subsequent papers [12, 13], these works have provided benchmark calculations for the motion of vapour bubbles near to rigid and free boundaries for a number of years. The only shortcomings due to the scheme employed by Taib are the omission in these studies of calculations very close to an infinite free surface, when very narrow liquid jets are observed to form; and in several cases near to the null-impulse state where unusual geometries arise and the calculations break down.

The implementation of the direct boundary integral method was later improved by Kucera [14, 15]. In this scheme, the surface geometry and potential thereon are described by a series of cubic-spline elements fitted through collocation points on the interface. Moreover, Best extended the boundary-integral formulation to examine the toroidal phase of an underwater explosion bubble which develops following liquid-jet impact [14]. This is achieved via the addition of a cut in the fluid domain to retain the singly connected topology post impact. In this early work, the cut is evolved in time as a material surface. This was later improved by Best who introduced a 'dynamic cut relocation algorithm' [16], in which the cut is taken to be a simple disk, any deformation of which may be ignored as it may then be arbitrarily remapped at each time step to this simple geometry. By careful labelling of surface nodes, the cut may be kept entirely within the column of fluid which threads the bubble; this being necessary in order that the cut does not cross the surface of the bubble. Furthermore, without the need to track the geometry of the cut, large computational savings are made.

The numerical scheme used in the current work is based on the techniques developed by Kucera and used with great success in [14, 15]. Also employed is the dynamic cut relocation algorithm due to [16] in order to permit the calculation of the toroidal phase of motion in close proximity to boundaries. In this study, we make further refinements, thus improving computational accuracy. A number of novel techniques are also developed to calculate physical quantities associated with the bubble, liquid jet and surrounding fluid.

2. Boundary-integral formulation

Herein we assume an inviscid and incompressible flow; thus, there exists some velocity potential, ϕ, for the flow domain around the bubble which satisfies Laplace's equation

$$\nabla^2 \phi = 0. \tag{1}$$

One of the well-known integral formulations of the solution to Laplace's equation may be written

$$c(\mathbf{p})\phi(\mathbf{p}) = \int_{\partial\Omega} \left(\frac{\partial \phi(\mathbf{q})}{\partial n} G(\mathbf{p}, \mathbf{q}) - \phi(\mathbf{q}) \frac{\partial G(\mathbf{p}, \mathbf{q})}{\partial n} \right) \mathrm{d}S, \tag{2}$$

where, for smooth boundaries, $c(\mathbf{p})$ is taken to be 1 if $\mathbf{p} \in \Omega \backslash \partial\Omega$ and $1/2$ if $\mathbf{p} \in \partial\Omega$. Here Ω is used to represent the flow domain and $\partial\Omega$, its boundaries. The Green's function $G(\mathbf{p}, \mathbf{q})$ is given by

$$G(\mathbf{p}, \mathbf{q}) = \frac{1}{4\pi |\mathbf{p} - \mathbf{q}|} + \frac{1}{4\pi |\mathbf{p} - \mathbf{q}'|}, \tag{3}$$

where $\mathbf{q}'$ is the image of the point $\mathbf{q}$ in the rigid boundary. The use of this image term removes the requirement to integrate over the infinite extent of the rigid boundary. Thus the required integration over the boundaries of the flow domain reduces to a surface integral over the surface of the bubble which we henceforth denote as S.

We move on from the well-established formulation for simply connected bubbles to consider the more complex formulation for toroidal bubbles in the next section.

3. The toroidal bubble: Reformulation of the integral equation

In this section, we consider the evolution of the bubble into the toroidal phase of motion. In doing this, the flow domain Ω changes topology from a singly connected to a doubly connected geometry via the liquid-jet impact. It is accepted that the fluid mechanics of jet impact are indeed complex, with effects due to liquid compressibility, viscosity and surface tension expected to play a rôle. However in order to gain some appreciation of the bubble motion, it is necessary we neglect these factors and seek a solution to Laplace's equation in the doubly connected flow domain.

In order to do this, we outline the work of Best [14] who considers the form of the boundary-integral equation immediately prior to and after liquid jet impact. We shall denote the surface over which jet impact takes place as T and denote the remainder of the bubble surface as S. Further, we shall denote the upper and lower surfaces of T by T_+ and T_- respectively, such that $T \equiv T_+ \cup T_-$. An outward unit normal is defined over the two surfaces and is represented by $\mathbf{n}_\pm$, where the subscript $\pm$ denotes quantities evaluated on $T_\pm$, respectively. We also introduce here the superscripts b and a which are used to signify a quantity immediately before and after jet impact. A schematic of the geometry can be found in Figure 1. We choose some point $\mathbf{t} \in T$ and write

$$\Delta\phi^{\mathrm{b}}(\mathbf{t}) = \phi_+^{\mathrm{b}}(\mathbf{t}) - \phi_-^{\mathrm{b}}(\mathbf{t}), \tag{4}$$

which in general is non-zero. Physically the change from a singly connected to doubly connected topology gives rise to a circulation, which we denote by Γ. This is deemed necessary in order that the Kelvin impulse is conserved. This circulation is obtained by integrating around any closed contour, C, to give
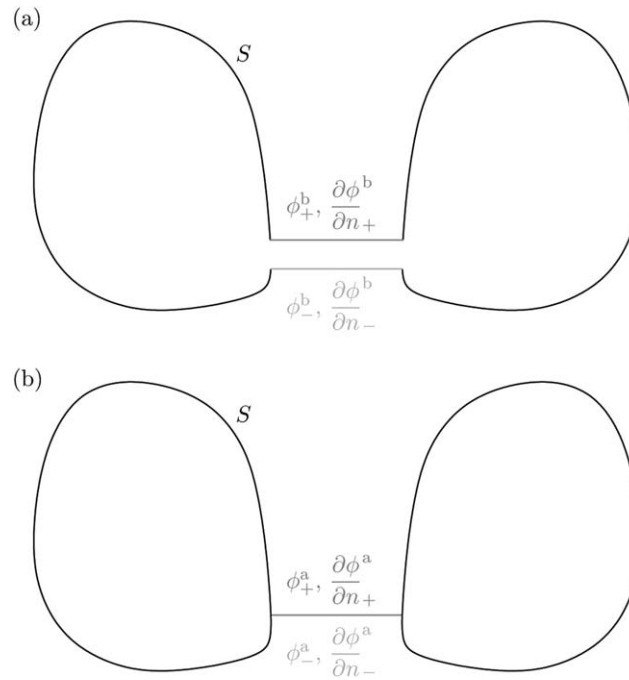
Figure 1. Schematic showing the transition to a toroidal bubble geometry: (a) an idealised bubble prior to jet impact with the appropriate potentials and normal velocities on T_+ and T_-; and (b) an idealised bubble following jet impact, again with the appropriate potentials and normal velocities on the cut.

$$\Gamma = \oint_C \mathbf{u} \cdot \mathbf{ds} = [\phi]_C, \tag{5}$$

where the notation $[\cdot]$ is used to signify a jump in potential. Immediately following impact, we know that

$$\phi_\pm^a(\mathbf{t}) - \phi_\pm^b(\mathbf{t}) = -\Pi_\pm/\rho, \tag{6}$$

on $T_\pm$, respectively, where $\Pi_\pm$ are the pressure impulses defined as $\Pi_\pm = \int p(\mathbf{t}_\pm)\mathrm{d}t$, an integral over the impact duration. Since $T_\pm$ experience a common pressure during impact, so the pressure impulse is constant, *i.e.* $\Pi_+ = \Pi_-$, and hence

$$\phi_+^a(\mathbf{t}) - \phi_-^a(\mathbf{t}) = \phi_+^b(\mathbf{t}) - \phi_-^b(\mathbf{t}). \tag{7}$$

Thus the jump in potential persists following impact and experiences no change in value. This may be written as

$$\Delta\phi^a(\mathbf{t}) = \Delta\phi^b(\mathbf{t}) = \Delta\phi(\mathbf{t}). \tag{8}$$

So the circulation Γ is dependent on the point $\mathbf{t}$, at which we begin and end our closed curve. For $\Delta\phi(\mathbf{t})$ non-uniform along the cut, the flow domain will be rotational. Only if $\Delta\phi(\mathbf{t})$ is uniform will we have irrotational flow with a constant circulation $\Delta\phi$ on any circuit. Reference [17] discusses the the nature of jet impact for high-velocity impacts for large Weber numbers, indicating a transition from vortex sheet formation to splashing, this latter phenomenon being particularly apparent in the following computations and in the relevant experimental studies reported in [18], one of which is illustrated in Figure 18.

During impact, the pressure inside the bubble, p_b is constant and so over the remainder of the bubble's surface S, the pressure impulse at any given point is

$$\Pi_S = \int p \, \mathrm{d}t = p_b \delta t, \tag{9}$$

where δt is the duration of the impact. If we now consider the duration of the impact $\delta t \to 0$ whilst p remains finite, then the pressure impulse, $\Pi_S = 0$. And hence we reason that during impact, there is no change in the potential on the remainder of the bubble surface S.

Hence we may formulate a boundary-integral equation for the toroidal phase of the bubble motion as

$$c(\mathbf{p})\phi(\mathbf{p}) = \int_S \left(\frac{\partial \phi(\mathbf{q})}{\partial n} G(\mathbf{p}, \mathbf{q}) - \phi(\mathbf{q}) \frac{\partial G(\mathbf{p}, \mathbf{q})}{\partial n} \right) \mathrm{d}S - \Delta\phi \int_T \frac{\partial G(\mathbf{p}, \mathbf{t})}{\partial n_+} \mathrm{d}S, \tag{10}$$

with $c(\mathbf{p})$ as defined following (2), provided $\mathbf{p} \notin T$. We note the additional term in (10) compared to (2) now requires integration over the impact surface, T.

In the following section, we outline the numerical scheme used to solve Equations (2) and (10) and advance the flow in time

4. Modelling the jet-formation phenomena

The method of solution may be summarised as follows. At some time t, both the shape of the bubble and the potential over its surface are presumed to be known, so Equation (2) (or, equivalently, Equation (10)) is a Fredholm integral equation of the first kind for the unknown normal velocity $\partial\phi/\partial n$. Its solution yields the normal velocity directly and the r- and z-components of velocity may be immediately resolved. Knowledge of the surface velocity allows us to advance both the surface geometry and potential so it is known at some time $t + \delta t$ shortly afterwards. Repetitions of this scheme allows us to advance the flow in time.

The surface geometry is advanced using the kinematic boundary condition, which for a given point $\mathbf{p}_i \in S$ is

$$\frac{\mathrm{D}\mathbf{p}_i}{\mathrm{D}t} = \mathbf{u}_i, \tag{11}$$

where $\mathbf{u}_i$ is the fluid velocity at the point $\mathbf{p}_i$. In a similar fashion, the rate of change of the velocity potential on the bubble surface is simply given by the potential's material derivative. By substituting for $\partial\phi_i/\partial t$ from Bernoulli's equation in this, we obtain the dimensionless dynamic boundary condition

$$\frac{\mathrm{D}\phi_i}{\mathrm{D}t} = \frac{1}{2}|\mathbf{u}_i|^2 + 1 - \alpha \left(\frac{V_0}{V} \right)^\kappa - \delta^2(z_i - \gamma), \tag{12}$$

where a subscript i denotes that quantity evaluated at the point $\mathbf{p}_i$. For a point on the surface of the bubble, we know both $\mathbf{u}_i$ from the solution of (2) and may readily calculate the bubble volume V. Hence Equations (11) and (12) may be integrated numerically to yield a new surface geometry and potential thereon.

In the above, lengths have been scaled with respect to the maximum bubble radius R_m^*, time with respect to $R_m^* \sqrt{\rho^*/\Delta p^*}$ and the pressure p^* by $(p^* - p_v^*)/\Delta p^*$, where $\Delta p^* = p_\infty^* - p_v^*$; p_∞^* and p_v^* being the hydrostatic and vapour pressures of the liquid, respectively. Where a star denotes a dimensional quantity. This leads to the following dimensionless parameters:
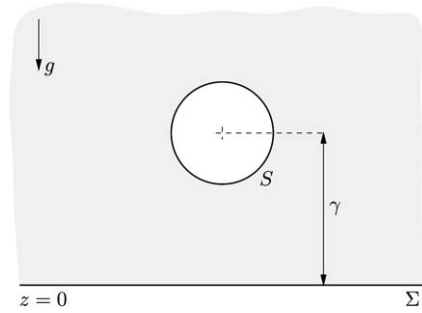
Figure 2. Schematic showing a bubble near a rigid boundary. The bubble is generated at a dimensionless distance γ from the boundary.

$$\alpha = \frac{p_0^*}{\Delta p^*}, \quad \gamma = \frac{h^*}{R_{\mathrm{m}}^*}, \quad \delta^2 = \frac{\rho^* g^* R_{\mathrm{m}}^*}{\Delta p^*}. \tag{13}$$

Here α is the compression ratio and is a measure of the initial high pressure, p_0^* within the bubble over the hydrostatic pressure at the inception depth. γ is the dimensionless standoff distance, the initial distance of the bubble centroid from the rigid boundary scaled with respect to maximum bubble radius; see Figure 2. Finally, δ is the buoyancy parameter and is a measure of how much the bubble rises under the influence of gravity. For the cavitation bubbles we consider henceforth, $\delta = 0$. Finally, we note that κ is the ratio of specific heats.

In order to solve Equation (2) in an axisymmetric geometry ($\partial/\partial\theta = 0$), we employ a collocation method, choosing a set of n (typically 50) nodes: $\mathcal{N}_1, \mathcal{N}_2, \ldots, \mathcal{N}_n$, on the surface of the half-bubble ($\theta = 0, r \geqslant 0$). We denote the cylindrical coordinates of the ith node by (r_i, z_i). We represent the surface of the bubble using a set of cubic splines, which are fitted through the node points to produce $n - 1$ surface elements, initially of equal arclength. The variation of the potential on the surface is also fitted as a cubic spline, whilst the unknown normal velocity, $\partial\phi/\partial n$ is assumed to vary linearly between two nodes with respect to the arclength. Hence we may form a system of linear equations, the direct solution of which yields the surface normal velocity.

4.1.   TOROIDAL-BUBBLE CALCULATIONS

Here we describe the changes to the numerical scheme of the previous section in order to allow for the transition to a doubly connected fluid domain. In our idealised model, the impact occurs at a single point, across which a jump in the potential of $\Delta\phi$ occurs. Since the impact occurs at a point, $\Delta\phi$ is uniform and hence no vortex sheet is formed. Initially the cut is a point, but through advancement of the flow, its geometry changes. Reference [16] shows the cut to be entirely arbitrary and it is hence remapped to a simple disk at each time step, resulting in huge computational savings. Physically, we would expect a loss of kinetic energy due to impact, manifesting itself as heat or acoustic radiation. However, for our idealised model with the restriction to a point impact, energy is conserved.

Up until the moment of impact, the scheme outlined above yields the geometry, potential and normal velocity on the boundaries, $\partial\Omega$ of our flow domain. Computationally, impact takes place when nodes $\mathcal{N}_1$ and $\mathcal{N}_n$ (which lie on the axis of symmetry) occur within some predetermined distance of each other. This yields the circulation of the successive flow as

$$\Delta\phi = \phi_n - \phi_1. \tag{14}$$

We recall over S (nodes $\mathcal{N}_2, \mathcal{N}_3, \ldots, \mathcal{N}_{n-1}$) the potential is unchanged, allowing evaluation of the fluid velocity as before.

Although we initially know the position of the cut, after this initial step we have no idea of where this meets the surface of the bubble. It is reasonable to assume that the regions of high curvature formed lead to the immediate smoothing of the bubble surface through the action of surface tension. Hence we remove nodes $\mathcal{N}_1$ and $\mathcal{N}_n$ from their position on the axis of symmetry and fit a smooth curve through the remaining nodes. These nodes are then introduced back into the surface of the bubble midway between nodes $\mathcal{N}_{n-1}$ and $\mathcal{N}_2$. This approach is given some credibility due to the spatially regular redistribution of nodes throughout preceding time steps. Hence the cut is taken as a disk of radius $r_1 \equiv r_n$, cutting the axis of symmetry at $z_1 \equiv z_n$, where the subscripts denote node number.

Having detailed the transitional scheme, we are now in a position to discuss the implementation of the boundary-integral method to solve Equation (10). This technique is almost identical to that discussed earlier, except for the appearance of the final term in this equation, which requires us to integrate over the cut. We note here that the coincident nodes $\mathcal{N}_1$ and $\mathcal{N}_n$ lie in $S \cup T$ and so the normal there is undefined; hence neither is $\partial\phi/\partial n$. For this reason, we choose not to collocate Equation (10) there, but do so only for the remaining $n-2$ nodes $\mathcal{N}_2, \mathcal{N}_3, \ldots, \mathcal{N}_{n-1}$. We do, however, require knowledge of the position of these nodes as it defines the spatial location at which ϕ is discontinuous. In order that we may track this point, it is essential the normal velocity there is known. This is evaluated by considering the interval between $\mathcal{N}_{n-1}$ and $\mathcal{N}_2$ as a single segment, along which the normal velocity is necessarily taken to vary linearly with respect to arclength as with the other surface elements.

4.2. DYNAMIC CUT RELOCATION

Here we detail the dynamic cut relocation algorithm due to Best [16]. This removes the need to follow the cut as a material surface as was previously done [14] by arbitrarily remapping the cut to a simple disc following each time step. In doing this, however, it becomes necessary to keep the point at which the cut meets the surface of the bubble within the column of liquid which threads the bubble. We take $\mathbf{t}$ to denote the point at which the cut meets the surface of the bubble prior to relocation and let $\mathbf{t}'$ denote the new position of the cut. We may then redefine the potential throughout the flow domain via the equation

$$\phi'(\mathbf{p}) = \phi(\mathbf{t}') + \int_{\mathbf{t}'}^{\mathbf{p}} \mathbf{u} \cdot \mathbf{ds}, \tag{15}$$

where a prime denotes a new quantity and $\mathbf{ds}$ is a line element taken over any curve in the fluid connecting $\mathbf{t}'$ with $\mathbf{p}$ which does not cross the newly relocated cut, T'. If the point $\mathbf{p}$ lies outside the region bounded by S, T and T', then the potential at $\mathbf{p}$ remains the same, that is

$$\phi'(\mathbf{p}) = \phi(\mathbf{t}') + [\phi(\mathbf{p}) - \phi(\mathbf{t}')] = \phi(\mathbf{p}). \tag{16}$$

However, if $\mathbf{p}$ lies inside this bounded region, the redefined potential is given by

$$\phi'(\mathbf{p}) = \phi(\mathbf{t}') + [\phi(\mathbf{p}) - \phi(\mathbf{t}') + \Delta\phi] = \phi(\mathbf{p}) + \Delta\phi, \tag{17}$$

and so the value of the potential there has changed by $\Delta\phi$.

4.3. SMOOTHING TECHNIQUES

In common with previous work in this field, during evolution of the flow, a high-frequency saw-tooth instability is found to occur. This is purely a facet of the numerical scheme and has been reduced through the implementation of high-order polynomial approximations to the elliptic integrals which are necessarily employed. These remove the requirement for smoothing where surface curvature is not too high.

In order to eliminate these instabilities, we choose to employ the method used by [19] which is based on a diffusion-like fourth-order PDE

$$\frac{\partial f}{\partial t} = -\lambda \frac{\partial^4 f}{\partial \xi^4},$$
(18)

which in effect damps higher-order modes, whilst leaving lower modes virtually unchanged. Here f is the function to be smoothed, ξ is arclength and λ is a 'diffusive' constant. Due to the occurrence of a diffusion parameter, this methods offers a variable degree of damping (beyond the frequency with which the smoothing is applied), so for bubbles over a certain distance from the boundary where the instabilities grow more slowly, a lesser degree of smoothing may be applied, thus improving accuracy.

In practice, we make finite-difference approximations to Equation (18) so that on a regularly spaced grid, the smoothed quantity $\bar{f}_j$ at node $\mathcal{N}_j$ is given by the five point formula

$$\bar{f}_j = f_j - D(f_{j-2} - 4f_{j-1} + 6f_j - 4f_{j+1} + f_{j+2}).$$
(19)

We note that the choice of $D = 1/16$ recovers the often used smoothing formula due to [20]. In practice we are able to adequately smooth the bubbles with a choice of $D < 1/16$ and for bubbles at a distance from the boundary, a choice of $D = 0{\cdot}01$ is fine. For further details on the choice of this method and the transition between Equations (18) and (19) see [21].

5. The calculation of physical quantities

In order that we may better understand the behaviour of the fluid flow around a bubble as it evolves in time, it is useful to calculate a number of physical quantities associated with the motion. Some, such as the internal pressure and volume of the bubble, are required in order to update the potential so calculations may proceed. Others, such as the centroid, Kelvin impulse and the partitioning of kinetic and potential energies, yield further insight into the fluid flow. Furthermore, calculating quantities associated with the liquid jet may further assist in the understanding of the non-spherical behaviour of the bubble.

Volume and pressure: The calculation of the volume requires integration to be performed over a number of volume elements, which are given in cylindrical polar coordinates by $dV = r\,dr\,d\theta\,dz$. The integrations with respect to r and θ may be performed analytically and the variable of integration changed to ξ, the arclength, the integration with respect to which is carried out numerically using Gaussian quadrature.

Once we have the volume of the bubble, this yields directly the pressure in the bubble as

$$p^* = p_{\mathrm{v}}^* + p_0^* \left(\frac{V_0^*}{V^*}\right)^{\kappa},$$
(20)

where p_{v}^* is the partial pressure due to non-condensible liquid vapour and p_0^* is the initial partial pressure due to an adiabatic gas within the bubble. In the case of a vapour bubble, this is zero, and hence the pressure within the bubble is constant.

Centroid: Due to the axisymmetric nature of the current work, the centroid will lie on the axis of symmetry, with the z-coordinate being given by

$$z_c^* = \frac{1}{V^*} \int_{V^*} z^* \, dV^*. \tag{21}$$

Kelvin impulse: As noted in [22], the Kelvin impulse "*...associated with a moving bubble presents much the same intuitive physical picture as the momentum of a rigid projectile in free space, and hence the feasibility of impact effects in the process of cavitation damage is immediately appreciated.*" Physically, the Kelvin impulse is a global measure of fluid momentum, and may be thought of as an instantaneous wrench which may be applied to the fluid in order to generate that motion from rest. For a more detailed discussion of the Kelvin impulse in relation to spherical bubble dynamics [23] and the references contained therein.

Due to the axisymmetric nature of our system, only the z-component is of interest, which is given by

$$I_z^* = -\rho^* \mathbf{e}_z \cdot \int_S \phi^* \mathbf{n} \, dS^*, \tag{22}$$

where $\mathbf{e}_z$ is a unit vector in the z-direction. We note the minus sign is due to the fact that the surface normal, $\mathbf{n}$ is directed outward with respect to the fluid; and so into the bubble.

In order to calculate the Kelvin impulse of a toroidal bubble, it is necessary to modify the above, so that integration is also performed across the cut. Hence $\int_S \mapsto \int_{S \cup T}$.

Kinetic energy: The calculation of energies associated with the motion of the bubble and surrounding fluid helps to provide further insight into the physical problems we consider. An expression for the kinetic energy due to the motion of the bubble is given by

$$E_k^* = \frac{\rho^*}{2} \int_S \phi^* \frac{\partial \phi^*}{\partial n} dS^*. \tag{23}$$

We note that in calculating the Kelvin impulse of a toroidal bubble, we are able to utilise the constant nature of the potential across the cut. However, it is obvious the normal velocity on the cut is not constant, and hence to calculate the kinetic energy of a toroidal bubble would require calculation of the normal velocity thereon. Due to the difficulty in doing this, a better estimate may be obtained by subtracting calculated values for the potential energy of compression from a reference energy.

We note that since energy is conserved in our model, the sum of the kinetic and potential energies of the system is constant and equals the initial energy of the system; except any energy losses due to errors in the numerical scheme. In the scheme employed herein, this may be shown to be a fraction of a percent [21].

Potential energy[1]: Here potential energy refers to the work done in changing the bubble's volume from its initial size, V_0 to some volume, $V(t)$; and not the gravitational potential energy which we omit due to our consideration of non-buoyant bubbles in this paper.[2] The potential energy of the bubble is given by

$$E_p^* = -\int_{V_0^*}^{V^*} (p^* - p_\infty^*) \, dV^*, \tag{24}$$

where p^* is the time varying pressure given by (20).

---

[1] We note this may be referred to as internal energy by some authors.

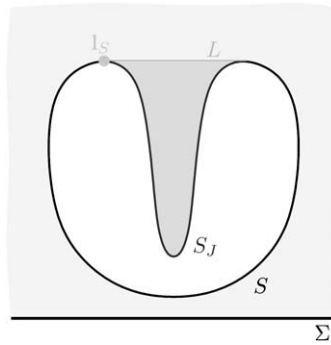[2] Techniques for the calculation of the gravitational potential energy are given in [21].

Figure 3. Schematic showing the volume of fluid which we call the jet. This is bounded by S_J, a subset of the surface of the bubble S and a flat circular lid L placed atop the bubble. The point $\mathbf{l}_S \in S_J \cap L$.

5.1. QUANTITIES CONCERNING THE LIQUID JET

Here we outline the techniques required in order to calculate the Kelvin impulse and kinetic energy for the volume of fluid which constitutes the liquid jet. For the purposes of our calculations, we consider the liquid jet to be the volume of fluid which may be bounded by some part of the surface of the bubble, $S_J \subset S$ and a circular lid, L placed on top of, or beneath, the bubble. See the schematic in Figure 3.

Kelvin impulse of the liquid jet: In calculating the Kelvin impulse of the liquid jet, we obtain an idea of the instantaneous wrench which would be required to set the liquid jet in motion from rest. We introduce at this stage the integral required to calculate the Kelvin impulse of the jet, which is

$$I_z^* = -\rho^* \mathbf{e}_z \cdot \int_{S_J \cup L} \phi^* \mathbf{n} \, dS, \tag{25}$$

which has the requirement that we integrate over $S_J \subset S$, which may be performed as for the Kelvin impulse of the bubble (with a little care where integration over a partial segment of the bubble surface is necessary), and across the circular lid, L. This requires the calculation of ϕ at points $\mathbf{l} \in L$ not on the surface of the bubble, but within the body of fluid surrounding the bubble. In order to calculate $\phi(\mathbf{l})$ at a point not too close to S, we appeal to Equation (2) where $c(\mathbf{p})$ is taken to be unity since $\mathbf{p} \equiv \mathbf{l} \in L \cap S'$ where all values on the right-hand side are known *a priori*.

However, some of the points of L do lie close to S. Indeed, during the earliest moments of jet formation, all points $\mathbf{l} \in L$ lie close to S, whence the singular nature of the Green's function leads to erroneous values for the calculated potential. Instead, we concentrate on calculating the Kelvin impulse of the jet at some time later once a more obvious jet may be observed; typically 30 iterations after the first occurrence of a concave portion of S. At this and subsequent times, much of L lies sufficiently far from S that the potential may be calculated accurately. We also know the potential at the point $\mathbf{l}_S \in S_J \cap L$. Crucially, we also know the derivative of ϕ along L, which is $\partial \phi / \partial r$; this is simply the r-component of surface velocity at $\mathbf{l}_S$. Using our values for ϕ on the central portion of L and the value of ϕ and its derivative at $\mathbf{l}_S$, we may fit a series of cubic-spline elements through the known data. Values for ϕ may then be calculated at points on L, close to S, where required. Hence the integral along L may be calculated using Gaussian quadrature.
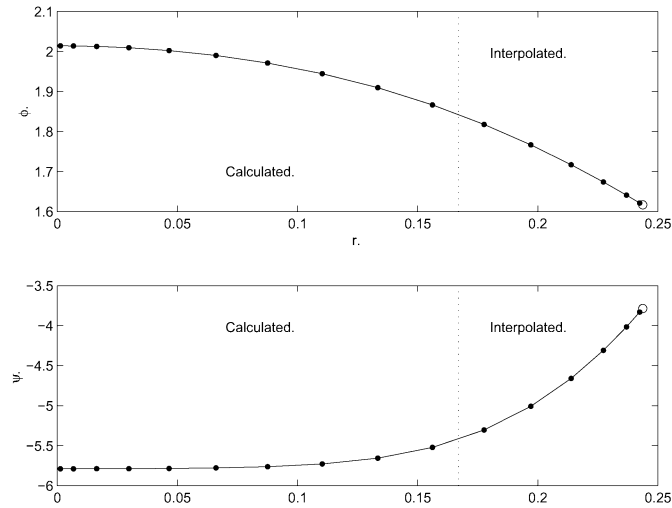
Figure 4. Potential and normal velocity across the lid L at the 30th time step following initial jet formation for bubble motion characterised by $\alpha = 500$, $\gamma = 1 \cdot 1$ and $\kappa = 1 \cdot 4$. Dots denote points at which data is required for the integration by Gaussian quadrature, with calculated values to the left of the vertical dotted line, and interpolated values to the right. Data at the point $\mathbf{l}_S$ is denoted by an open circle.

Figure 4 shows an example of the variation in potential and normal velocity across L at the 30th time step following the initial jet formation in a typical cavitation bubble. We note that data is calculated explicitly using the boundary-integral method at twelve points: the first on the axis of symmetry, the last at $\mathbf{l}_S$, the remaining ten at the ten abscissas nearest the axis of symmetry which are required for numerical integration using sixteen point Gaussian quadrature. Splines are fitted to this calculated data and the further six values required for quadrature at the end nearest $\mathbf{l}_S$ calculated by interpolation. We note the non-constant nature of these quantities which shows these techniques to be necessary.

Kinetic energy of the liquid jet: The techniques for calculating the Kelvin impulse of the liquid jet detailed above are readily extended to calculate the kinetic energy therein, and is given by

$$E_{\text{k}}^* = \frac{\rho^*}{2} \int_{S_J \cup L} \phi^* \frac{\partial \phi^*}{\partial n} \mathrm{d}S. \tag{26}$$

We note the need to also calculate the normal velocity, $\partial \phi / \partial n$ on L. Again, values for ϕ and $\partial \phi / \partial n$ are calculated on the central portion of L and at the point $\mathbf{l}_S$ which also lies on the surface of the bubble. Despite the fact that we do not know the derivative of $\partial \phi / \partial n$ at $\mathbf{l}_S$, splines may still be fitted to the data using not-a-knot end conditions at the outer end of L, whilst retaining the prescribed derivative $\partial \phi / \partial r = 0$ on the axis of symmetry. Even with the use of the not-a-knot condition, we are confident that the splines adequately capture the behaviour of $\partial \phi / \partial n$ along L, since any errors are readily noticeable in the final value for the kinetic energy of the jet and may be removed after inspection.

5.2. INSTANTANEOUS PRESSURE AND VELOCITY FIELDS

One aspect in which our numerical calculations offer physical insight beyond that afforded our experimental colleagues is in the calculation of quantities throughout the flow domain.

Whilst it is possible to record information at the boundaries, such as the pressures thereon [24], it is not easily possible to record this data within the body of the fluid. Especially since regions of interest are often in close proximity to the bubble, where recording devices may have a significant influence on the motion of the bubble. Furthermore, where information is recorded at the boundary, the range of cases considered may be limited due to damage caused to, for example, pressure transducers by the violent collapse of the bubble.

Velocity-field calculations: Here we note the r- and z-components of fluid velocity are given by $\partial\phi/\partial r$ and $\partial\phi/\partial z$, respectively. We choose to calculate these derivatives using a five-point formula. Furthermore, since the fluid velocities are required for the calculation of the fluid pressure, the spatial steps between these five points are taken to be the average of the temporal steps between the preceeding two and following two time steps.

Finally, we note that, in order that erroneous values are not calculated either inside or close to the surface of the bubble, a narrow region (typically of non-dimensional width 0·01) is created around the bubble. We then omit points through the calculation of a winding number.

Pressure-field calculations: In order to calculate the pressure throughout the body of the fluid, we use the dimensionless Bernoulli pressure equation

$$p = 1 - \frac{\partial\phi}{\partial t} - \frac{1}{2}|\nabla\phi|^2 - \alpha\left(\frac{V_0}{V}\right)^{\kappa} - \delta^2(z - \gamma), \tag{27}$$

which requires the fluid velocity at the point in question (as calculated above) and also the time derivative of the potential, which is again calculated using a five-point formula.

6. Numerical calculations: Vapour and gas bubbles near a rigid boundary

We briefly consider the case of a vapour bubble close to a rigid boundary before studying the motion of bubbles with a gas–vapour content, again near to a rigid boundary. For this latter problem we thoroughly examine the physical quantities associated with the motion in order to gain further physical insight. Finally, we compare our calculations against a recent experimental study wherein the motion of the bubble is recorded using high-speed photography at an elevated angle above a rigid boundary.

We begin the discussion of our results concerning bubble motion near boundaries by considering one example of the motion of a vapour bubble near a rigid boundary to be complemented by studies of the motion of a bubble with a mixed vapour and gas content near to a rigid boundary. The inclusion of a gaseous content in the bubble allows a much more detailed examination of the physical quantities associated with motion to be undertaken.

Figure 5 shows the motion of a vapour bubble generated at a standoff distance, $\gamma = 1$ from a rigid boundary. In Figure 5 we present half-rendered bubble shapes for both the pre-toroidal and toroidal phases of motion. Frames 1 and 2 show the bubble at the start of our calculations and at maximum volume, respectively. We note the flattening of the underside of the bubble at maximum volume due to the close proximity of the boundary. Frames 3–6 show the collapse phase up until the time of liquid-jet impact. Due to the Bjerknes force of attraction, both the migration of the centroid and the direction of the liquid jet are directed towards the boundary. Following jet impact (Frame 7 onwards), the resulting circulation channels fluid through the centre of the bubble. This fluid then impacts against the boundary and is forced outward along it. Due to the continued collapse of the bubble, fluid continues to rush in from the far-field. Where the opposing flows meet, a 'splash' of liquid is thrown up inside the
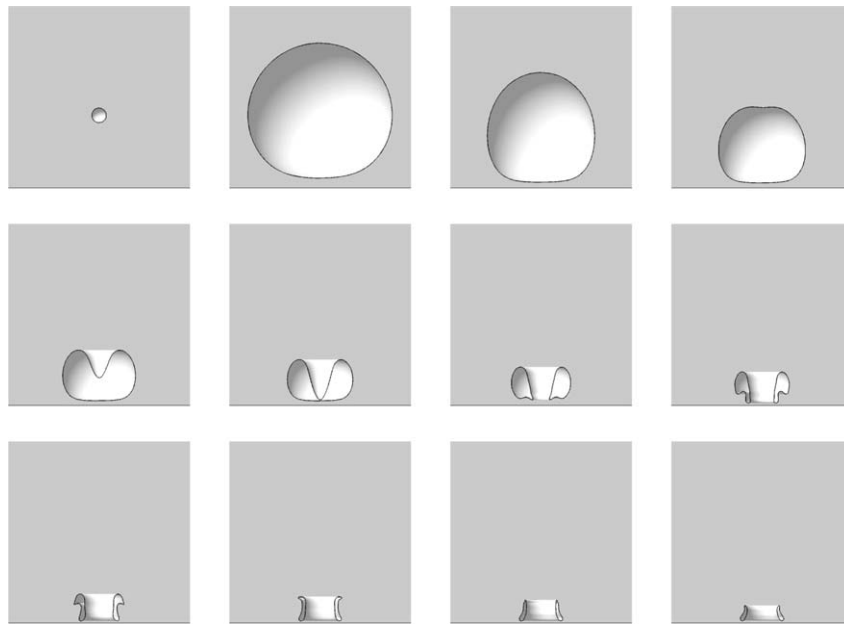
Figure 5. Half-rendered bubble shapes showing the motion of a vapour bubble near a rigid boundary with $\gamma = 1.0$. Horizontal and vertical axes are: $r \leqslant 1.25$, $0 \leqslant z \leqslant 2.5$, hence the rigid boundary is visible at the bottom of each frame. Dimensionless times are 0·0015, 1·0536, 1·7747, 1·9565, 2·0488, 2·0850, 2·0995, 2·1071, 2·1212, 2·1387, 2·1478 and 2·1518, respectively.

bubble. Further consideration is given to the splash phenomenon in the paper by [17]. Figure 6 contains velocity vectors and pressure contours within the body of the fluid at four instants during the motion, in which the region of high pressure which forms above the bubble and drives the flow may be seen. Following jet impact, a region of higher pressure forms on the rigid boundary, which then continues to spread outwards as the flow evolves. The circulation around the bubble may be observed in Frames 3 and 4.

Henceforth we present a much fuller discussion of the motion of a cavitation bubble containing both non-condensible liquid vapour and gas near to a rigid boundary. Although in many cases a good agreement with experiments may be achieved by simply considering the motion of a vapour bubble, key features of the motion around minimum volume, where phenomena are associated with the compression of gas within the bubble, may be lost. In particular, the speed of the liquid jet during final collapse may be greatly affected. This is of consequence where bubbles of highly disparate maximum bubble radii, and hence period of oscillation, are considered.

It is of interest to consider the motion of cavitation bubbles generated over a range of standoff distances from a rigid boundary; henceforth we primarily consider the compression ratio $\alpha = 100$. In order to give an idea of the bubble geometries which develop, we consider the shape of the bubble at the time of liquid jet impact. Half-rendered bubble shapes for $\alpha = 100$, and standoff distances over the range $\gamma = 0.7 - 6.0$ are presented in Figure 7. For standoff distance of $\gamma = 1.0$ and below, the bubble is characterised by a wide liquid jet and flattened underside, which becomes more pronounced as the bubble is initiated closer to the boundary. As the point of initialisation is moved further from the boundary, the expansion phase quickly becomes almost spherical in nature as the influence of the boundary lessens.
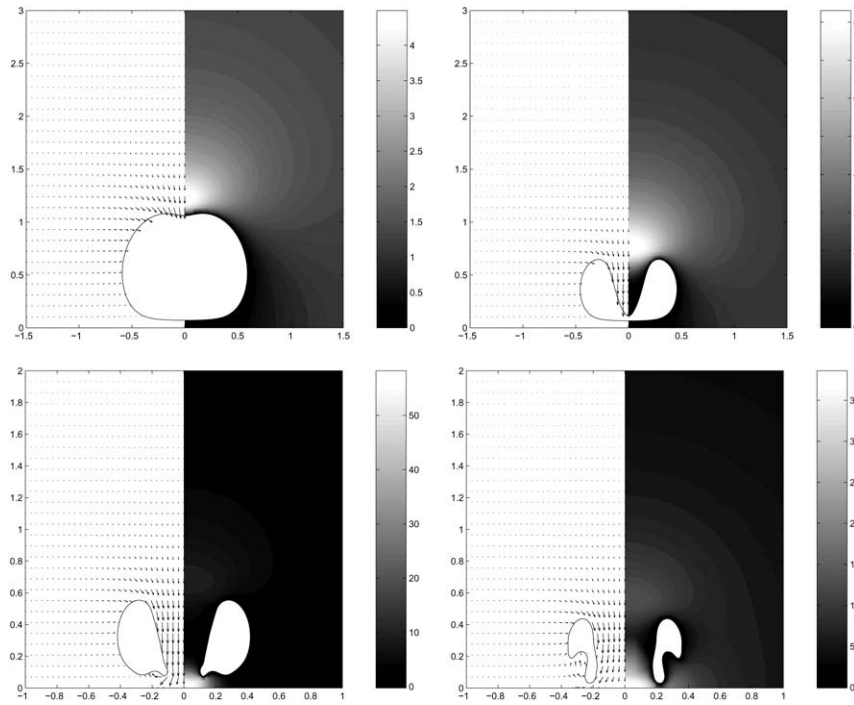
Figure 6. Velocity vectors and pressure contours showing the motion of a vapour bubble near a rigid boundary with $\gamma = 1 \cdot 0$. Times are $1 \cdot 9628$, $2 \cdot 0802$, $2 \cdot 0958$ and $2 \cdot 1112$, respectively.

Furthermore, due to the decrease in the Bjerknes force of attraction, the bubble attains a progressively smaller volume at the time of jet impact upto a certain standoff distance. Beyond this critical distance, the bubble reaches minimum volume and begins to re-expand whilst simply connected. For a further range of γ values, the liquid jet will impact on the opposing face of the bubble during re-expansion. Then beyond this second critical standoff, jet impact will not occur, at least during the first oscillation of the bubble. One other feature which may be regarded as a function of standoff distance is breadth of the liquid jet, which becomes first proportionally wider, then much thinner as γ is increased.

Corresponding calculations for $\alpha = 1000$ (not presented) yield very similar bubble shapes over the range $\gamma = 0 \cdot 75 - 1 \cdot 5$ indicating the predominant influence on motion in this range is the boundary and not the internal pressure of the bubble. For larger standoff distances, the volumes at jet impact are typically smaller and the jets which form are wider than those observed for $\alpha = 100$ at a given standoff distance. For corresponding calculations for $\alpha = 1000$ to results presented in this paper, see [21].

The evolution of the bubble volume upto the time of jet impact for the compression ratio $\alpha = 100$ and for a range of standoff distances is shown in Figure 8. We note the afore-mentioned decrease in bubble volume at the time of jet impact as γ increases. We note the slight upturn at the end of the curve for $\gamma = 2 \cdot 5$, thus showing that the bubble is starting to re-expand. At $\gamma = 7 \cdot 5$, the bubble re-expands significantly prior to jet impact.

We consider the motion of the bubble centroid for a number of standoff distances at the compression ratio $\alpha = 100$ in Figure 9. For bubbles formed close to the boundary, the expansion phase is characterised by upward motion of the centroid as the bubble expands, displacing fluid as it does so. As the point of initiation is moved further from the boundary, the bubble
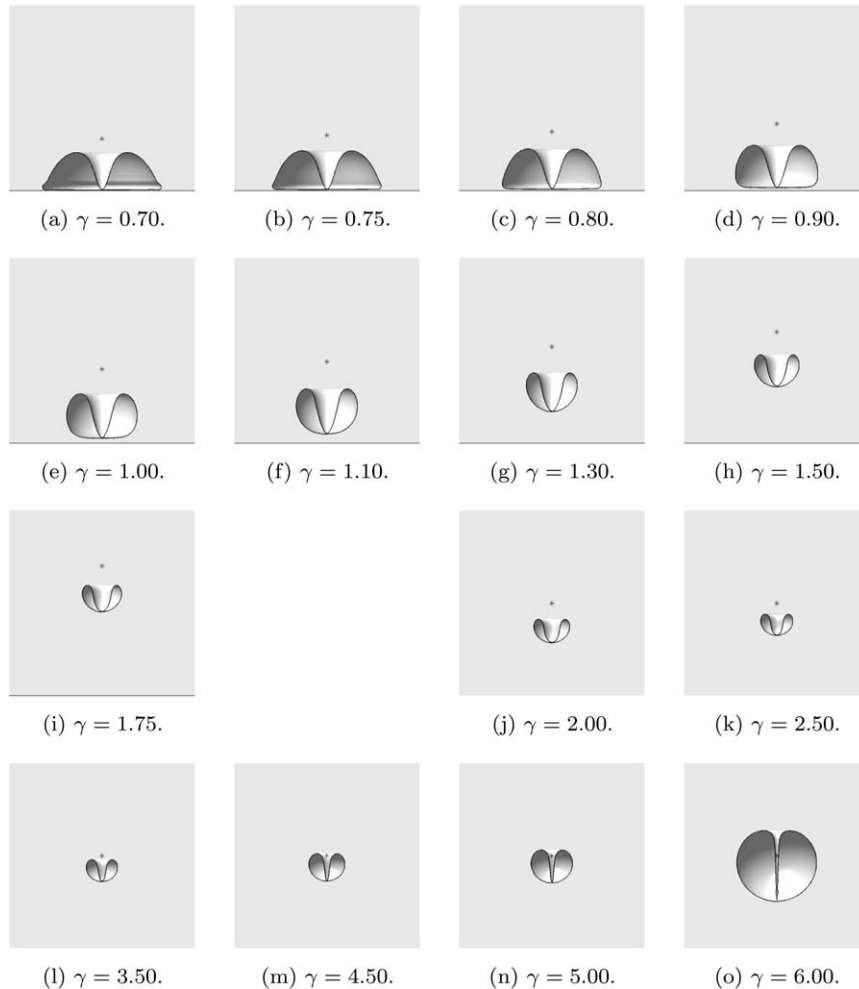
Figure 7. Half-rendered bubble shapes showing the geometry of a cavitation bubble ($\alpha = 100$) above a rigid boundary for a range of standoff distances at the time of jet impact. Horizontal and vertical axes are: (a) through (i) $r \leqslant 1.25$, $0 \leqslant z \leqslant 2.5$; and (j) through (o) $r \leqslant 1.25$, $|z - \gamma| \leqslant 1.25$. The black star denotes the point of initialisation. The boundary is visible at the bottom of the frames (a) through (i).

(a) $\gamma = 0.70$. (b) $\gamma = 0.75$. (c) $\gamma = 0.80$. (d) $\gamma = 0.90$. (e) $\gamma = 1.00$. (f) $\gamma = 1.10$. (g) $\gamma = 1.30$. (h) $\gamma = 1.50$. (i) $\gamma = 1.75$. (j) $\gamma = 2.00$. (k) $\gamma = 2.50$. (l) $\gamma = 3.50$. (m) $\gamma = 4.50$. (n) $\gamma = 5.00$. (o) $\gamma = 6.00$.

expands more uniformly about its point of inception; though there is still some movement away from the boundary for $\gamma = 2.5$. During collapse, the Bjerknes force of attraction draws the bubble towards the boundary, this downward centroid movement increases rapidly as the jet forms and bubble volume is lost progressively from the top down at a rapid rate. For bubbles formed at standoff distances greater than about 4.0, there is little centroid movement until the jet forms, after which there is a very rapid downward movement. We note centroid motion for $\gamma = 7.5$, which remains almost stationary until just prior to minimum volume, when it experiences rapid downward movement due to the initial formation of the jet. As previously noted, the bubble starts to re-expand before this jet may impact on the opposing face of the bubble, though the gentle downward trend in this curve is consistent with the jet finally impacting. We note such behaviour is observed in buoyant spherical bubble models.

Figure 10 shows our calculations for the Kelvin impulse for a range of standoff distances. The strong influence of the boundary on the bubbles formed closest to it is characterised by the
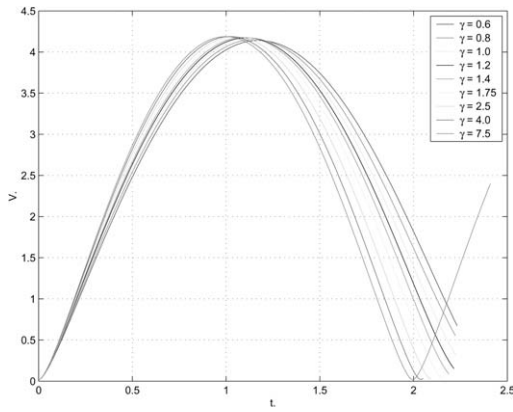
Figure 8. Evolution of the volume of a cavitation bubble ($\alpha = 100$) generated above a rigid boundary for a range of standoff distances up until the time of jet impact.
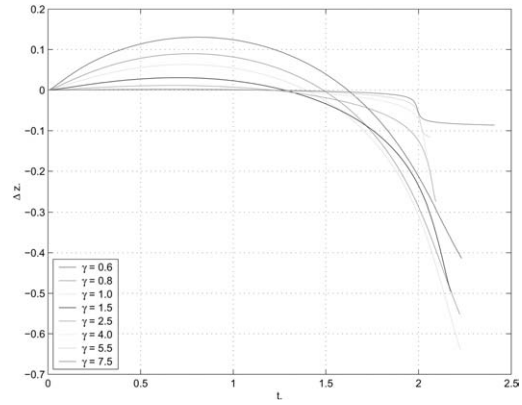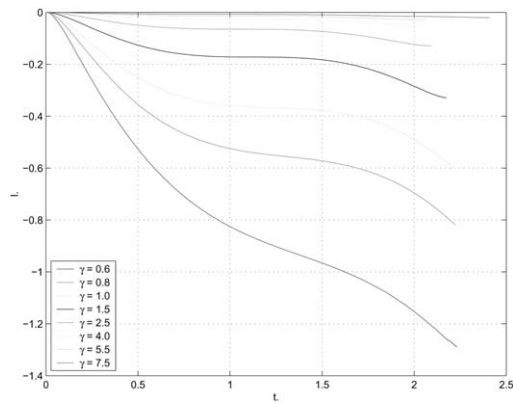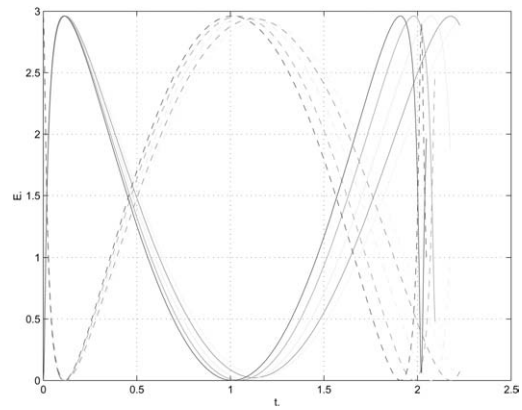

Figure 9. Changes in centroid position for the motion of a cavitation bubble ($\alpha = 100$) generated above a rigid boundary for a range of standoff distances up until the time of jet impact.

Figure 10. The Kelvin impulse associated with the motion of a cavitation bubble ($\alpha = 100$) generated above a rigid boundary for a range of standoff distances up until the time of jet impact.

Figure 11. The kinetic and potential energies associated with the motion of a cavitation bubble ($\alpha = 100$) generated above a rigid boundary for a range of standoff distances up until the time of jet impact. Total energy = 2·9615. See Figure 12a for legend.

larger magnitudes of the Kelvin impulse; the negative values indicate a downward influence. Also of note are the more rapid increases in the impulse during the early expansion phase and final collapse when the liquid jet forms. Physically, we recall the Kelvin impulse may be thought of as an instantaneous wrench which would generate the motion from rest and so the trends noted here are indicative of rapidly changing fluid momentum near the bubble during early expansion and final collapse.

Figures 11 and 12 shows the kinetic and potential energies associated with the motion of bubbles formed over a range of γ values for $\alpha = 100$. In Figure 11 we show the energies calculated up until the time of liquid jet impact. We note the rapid change from potential energy to
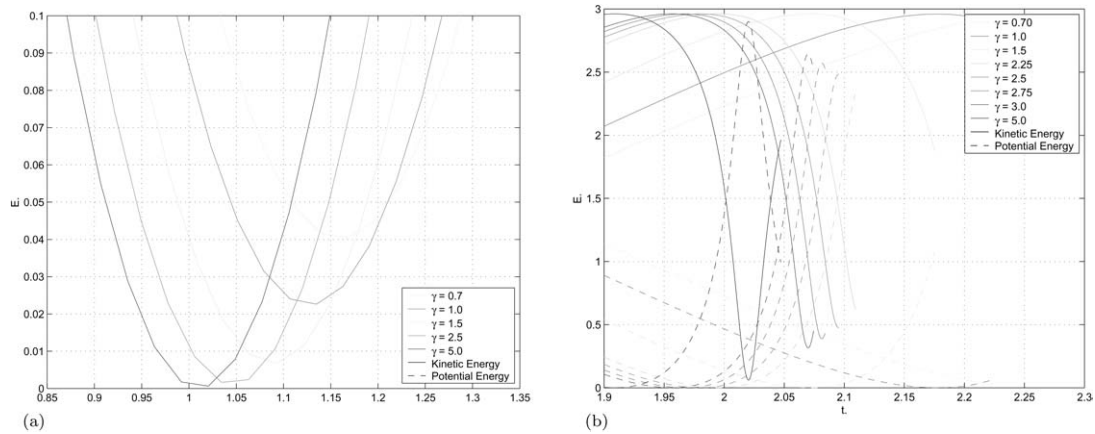
Figure 12. The kinetic and potential energies associated with the motion of a cavitation bubble ($\alpha = 100$) generated above a rigid boundary for a range of standoff distances up until the time of jet impact: (a) first minimum in kinetic energy associated with maximum bubble volume; and (b) second minimum associated with minimum volume. Total energy = 2·9615.

kinetic energy during the earliest moments of the lifetime of the bubble as the high pressures within the bubble rapidly accelerate the fluid-gas interface, and the reverse process as the high surface velocities which develop during collapse re-compress the gas within the bubble. Figure 12a shows the first minimum in kinetic energy which corresponds to maximum bubble volume.[3] We note for bubbles formed at some distance from the boundary this minimum is virtually zero, hence the entire surface of the bubble has zero velocity which will only occur if the bubble behaves spherically. For bubbles formed close to the boundary, this minimum is non-zero which is indicative of some part of the surface of the bubble being in motion at all times, so even through the stable expansion phase, the bubble has developed non-spherical attributes. The non-smooth nature of these curves is due to relatively large time steps which may be taken when the surface of the bubble is slowly moving. The second minimum in kinetic energy is shown in Figure 12b, and corresponds to minimum bubble volume. Here we note the minimum values of the kinetic energy are all non-zero indicating highly non-spherical behaviour, which should be expected following collapse. Finally we note the increases in kinetic energy for $\gamma = 2 \cdot 75$ and $3 \cdot 0$, following their respective minima. This further indicates the bubble is re-expanding.

We now proceed to discuss our calculations concerning the kinetic energy and Kelvin impulse of the liquid jet. Having just concluded our discussions of the energy of the bubble as a whole, it is pertinent to discuss the kinetic energy of the jet first. Figure 13 shows the percentage of the total energy which is manifested as kinetic energy within the liquid jet. We recall the energy is calculated from a time shortly following jet formation[4] (which in Figure 13 occurs in the dimensionless time range 2·02–2·13), up until the time of jet impact ($t = 2 \cdot 05$– 2·23). For $\alpha = 100$ we note the largest percentage of kinetic energy within the jet is 31% at the time of jet impact and occurs at a standoff distance of $\gamma = 1 \cdot 2$. For bubbles generated closer to the boundary, this percentage decreases steadily as γ decreases. For bubbles generated further from the boundary, we have a steady decrease in this percentage. One interesting feature of

[3]Since energy is conserved, minimum kinetic energy corresponds to maximum potential eneregy. Hence the pressure within the bubble will be at a minimum, which occurs at maximum volume.

[4]Typically 30–40 iterations after the appearance of a concave section at the upper pole of the bubble.
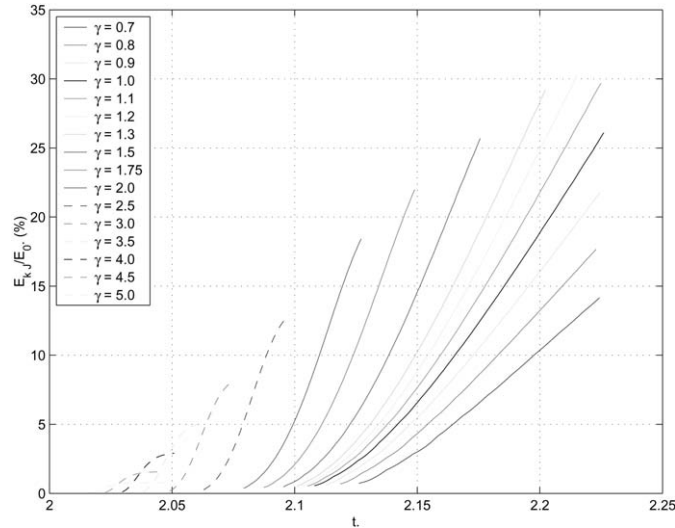
Figure 13. Percentage of the total energy of motion which is manifested as kinetic energy within the liquid jet of a cavitation bubble ($\alpha = 100$) for a range of standoff distances from a time shortly following jet formation up until the time of jet impact. We note the variation in total impulse is shown in Figure 9.
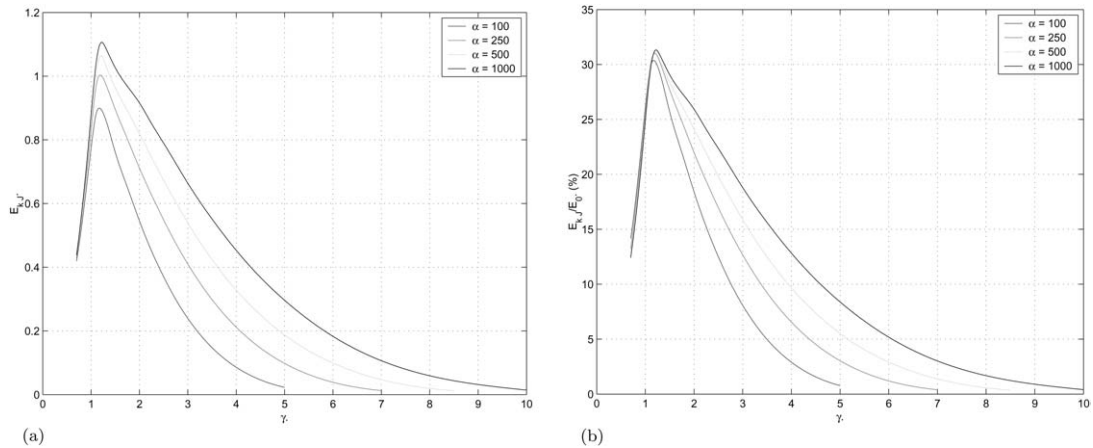

Figure 14. Kinetic energy within the liquid jet at the time of jet impact over a range of standoff distances and for several compression ratios: (a) dimensionless energy units; and (b) as a percentage of the total energy of motion.

these calculations may be seen by looking at the curve for $\gamma = 4\cdot5$ or $\gamma = 5\cdot0$ in Figure 13. Here the kinetic energy in the jet reaches a fixed percentage of the total energy, then becomes almost constant. This may be attributed to the deceleration of the liquid within the jet due to compression of gas within the bubble as its volume decreases, then subsequent acceleration of the remaining surface of the bubble (which does not bound the liquid jet) due to high internal pressures.

Figure 14 shows the kinetic energy in the liquid jet at the time of jet impact for several compression ratios and over a range of standoff distances. We see that for compression ratios from $\alpha = 100$ to $\alpha = 1000$, the maximum amount of energy within the jet occurs at a standoff distance of $\gamma \approx 1\cdot2$. For larger compression ratios, there is a greater amount of energy within the jet, yet the percentage of the total is approximately equal at around 31%–32%. For γ
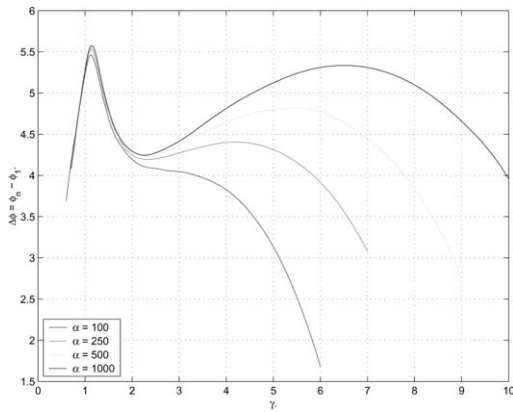
Figure 15. Circulations formed at jet impact over a range of standoff distances and for several compression ratios.
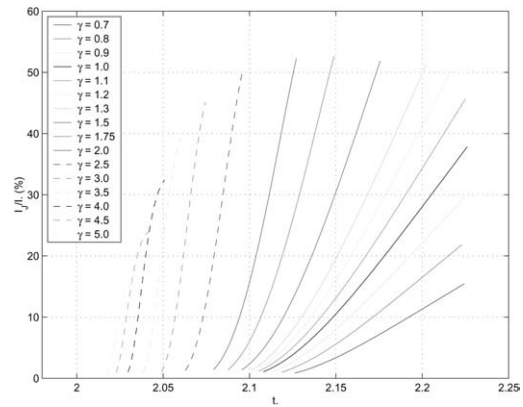

Figure 16. Percentage of the instantaneous total Kelvin impulse of a cavitation bubble ($\alpha = 100$) within the liquid jet for a range of standoff distances from a time shortly following jet formation up until the time of jet impact.

values smaller than this we also see that the percentage of total energy contained within the liquid jet is roughly equal over the range of compression ratios considered. This is due to the strong influence of the boundary over the motion as noted earlier. This may also be seen if we consider the circulations formed following jet impact in Figure 15, where we note the circulations are roughly equal over the range of $\alpha = 100$–1000 up to $\gamma \approx 1.75$.

Finally we consider the Kelvin impulse within the liquid jet. This is shown in Figure 16 as a percentage of the instantaneous Kelvin impulse of the bubble. Upto $\gamma \approx 1.5$, these percentages are roughly equal for $\alpha = 100$ and $\alpha = 1000$. As γ increases beyond this value, we see that over 50% of the Kelvin impulse (a measure of the fluid momentum) is contained within the liquid jet. For bubbles at a large distance from the boundary, this starts to decrease as the influence of the boundary decreases.

One recent experimental study which employs a number of novel visualisation techniques is that of [18] and which provides a helpful comparison to our computational studies. Of particular interest are a number of experimental photograph series which are viewed at an elevated angle of 45° above the boundary. This permits the examination of radial instabilities which may form during the unstable collapse phase. Further these photograph series are captured using an ultra-high speed camera capable of upto 100 million frames per second allowing detailed study of the toroidal phase of motion which occurs on comparatively short time-scales. Figure 17 shows calculations for the motion of a laser-induced cavitation bubble characterised by the parameters $\alpha = 600$, $\gamma = 0.8$ and $\kappa = 1.4$. In Figure 17 we follow the motion from initial bubble formation upto maximum volume (Frames 1–3) then through to liquid jet impact (Frame 7). Although less obvious than in results viewed in profile, we note that during the expansion phase, the underside of the bubble is flattened against the rigid boundary. Following jet impact, a toroidal bubble geometry is formed (Frame 8) and a liquid splash thrown up inside the bubble. The motion of this splash may be followed as it is driven towards the outer edge of the bubble and is visible as the lighter coloured ring at the base of the bubble in Frames 9–15. Calculations cease when this splash meets the outer edge of
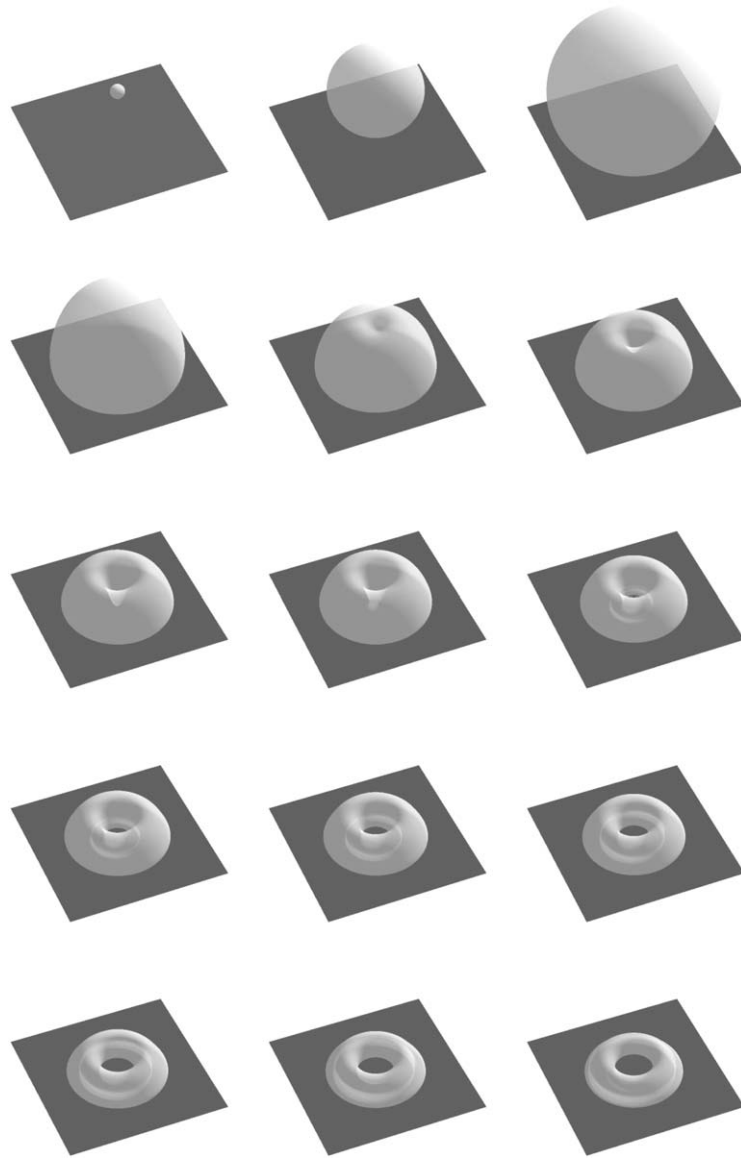
Figure 17. Rendered transparent bubble shapes showing the motion of a cavitation bubble near a rigid boundary for the parameters $\alpha = 600$, $\gamma = 0.8$ and $\kappa = 1.4$. The square portion of the rigid boundary shown is $2R_{\mathrm{m}} \times 2R_{\mathrm{m}}$ and angle of elevation is $45°$. Times are 0·0000, 0·1505, 1·1082 (maximum volume), 1·8952, 2·0724, 2·1213, 2·1654 (jet impact), 2·1654, 2·2016, 2·2100, 2·2195, 2·2298, 2·2408, 2·2518 and 2·2615, respectively.

the bubble. High-speed experimental photographs for this case are reproduced in Figure 18, wherein jet impact is visible around Frame 4–5. We note the liquid splash is clearly visible as a darkened ring at the base of the bubble in the third row of images in this figure. It is somewhat unclear as to how the splash develops as it reaches the outer edge of the bubble, though it is likely surface-tension effects act to prevent this becoming so large as to meet the outer surface of the bubble as in our calculations. In the final three rows of experimental images, the bubble reaches minimum volume as a narrow toroidal ring, following which it begins to re-expand. We note surface instabilities around the bubble are clearly visible at this stage.
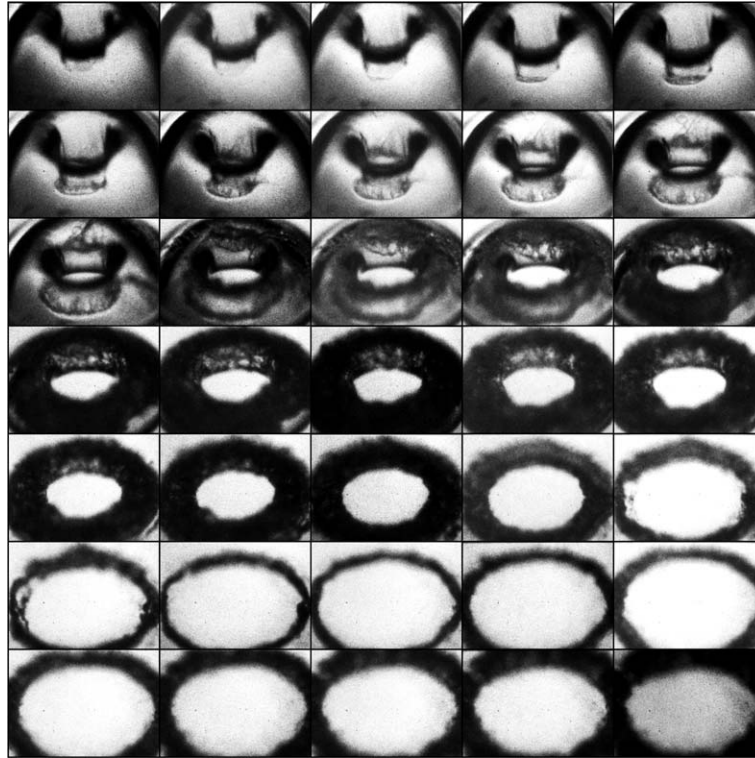
Figure 18. The final stages of collapse and rebound of a laser-generated cavitation bubble near a rigid boundary characterised by $\alpha = 600$, $\gamma = 0.8$, $\delta = 0.0$ and $\kappa = 1.4$. Motion is viewed from an angle of $45°$ above the rigid boundary. Reproduced with permission from [18].

7. Concluding remarks

In this paper, we have outlined a boundary-integral scheme for the calculation of both the pre-toroidal and toroidal phases of motion of a single bubble near to a rigid boundary. Using non-standard smoothing techniques and a fourth-order time integration scheme, numerical energy losses have been reduced, resulting in more accurate calculations. Further physical insight into a range of problems has been gained through the calculation of physical quantities associated with the bubble and surrounding fluid. Several of these, most notably the Kelvin impulse and kinetic energy associated with the liquid jet, have not previously been examined and provide new information about the highly non-spherical aspects of the motion in close proximity to the rigid boundary. Recent visualisation techniques [18] have provided interior details on bubble shape in agreement with calculations. This is in contrast to earlier experiments wherein motion is generally recorded in profile, requiring us to infer interior behaviour. This is an important validation of the reliability of the current code in calculating the violent behaviour of collapsing cavitation bubbles, especially those involving high-speed liquid jets.

References

1. Lord Rayleigh, On the pressure developed in a liquid during the collapse of a spherical cavity. *Phil. Mag.* 34 (1917) 94–98.
2. C. Herring, Theory of the pulsations of the gas bubble produced by an underwater explosion. In: G.K. Hartmann and E.G. Hill (eds.), *Underwater Explosion Research, Vol. II*. Washington: Office of Naval Research (1950).
3. J.B. Keller and I.I. Kolodner, Damping of underwater explosion bubble oscilliations. *J. Appl. Phys.* 27 (1956) 1152–1161.
4. A. Prosperetti and A. Lezzi, Bubble dynamics in a compressible liquid. Part 1. First order theory. *J. Fluid Mech.* 168 (1986) 457–478.
5. B.D. Storey and A.J. Szeri, Water vapour, sonoluminescence and sonochemistry. *Proc. R. Soc. London* A456 (2000) 1685–1709.
6. B.D. Storey and A.J. Szeri, A reduced model of cavitation physics for use in sonochemistry. *Proc. R. Soc. London* A457 (2001) 1685–1700.
7. A.J. Szeri, B.D. Storey, A. Pearson and J.R. Blake, Heat and mass transfer during the violent collapse of non-spherical bubbles. *Phys. Fluids.* 15 (2003) 2576–2586.
8. M. Lenoir, Calcul numérique de l'implosion d'une bulle de cavitation au voisinage d'une paroi ou d'une surface libre. *J. Mécanique* 15 (1976) 725–751.
9. L. Guerri, G. Lucca and A. Prosperetti, A numerical method for the dynamics of non-spherical cavitation bubbles. In: D.H. LeCroisette (ed.), *Proceedings of the 2nd International Colloquium on Drops and Bubbles*. Pasadena (CA): Jet Propulsion Laboratory (Publ. 82–7) (1982) pp. 175–181.
10. A. Prosperetti and G. Seminara, Linear stability of a growing or collapsing bubble in a slightly viscous liquid. *Phys. Fluids* 21 (1978) 1465–1470.
11. B.B. Taib, *Boundary Integral Method Applied to Cavitation Bubble Dynamics*. PhD thesis. The University of Wollongong, Australia (1985) 108pp.
12. J.R. Blake, B.B. Taib and G. Doherty, Transient cavities near boundaries. Part 1. Rigid boundary. *J. Fluid Mech.* 170 (1986) 479–497.
13. J.R. Blake, B.B. Taib and G. Doherty, Transient cavities near boundaries. Part 2. Free surface. *J. Fluid Mech.* 181 (1987) 197–212.
14. J.P. Best, *The Dynamics of Underwater Explosions*. PhD thesis. The University of Wollongong, Australia (1991) 184pp.
15. J.P. Best and A. Kucera, A numerical investigation of non-spherical rebounding bubbles. *J. Fluid Mech.* 245 (1992) 137–154.
16. J.P. Best, The rebound of toroidal bubbles. In: J.R. Blake, J.M. Boulton-Stone and N.H. Thomas (eds.), *Bubble Dynamics and Interface Phenomena*, Vol. 23 of *Fluid Mechanics and its Applications*. Dordrecht: Kluwer Academic Publishers (1994) pp. 405–412.
17. R.P. Tong, W.P. Schiffers, S.J. Shaw, J.R. Blake and D.C. Emmony, The rôle of 'splashing' in the collapse of a laser-generated cavity near a rigid boundary. *J. Fluid Mech.* 380 (1999) 339–361.
18. O. Lindau and W. Lauterborn, Cinematographic observation of the collapse and rebound of a laser-produced cavitation bubble near a wall. *J. Fluid Mech* 479 (2003) 327–348.
19. T.S. Lundgren and N.N. Mansour, Oscillations of drops in zero gravity with weak viscous effects. *J. Fluid Mech.* 194 (1988) 479–510.
20. M.S. Longuet-Higgins and E.D. Cokelet, The deformation of steep surface waves on water I. A numerical method of computation. *Proc. R. Soc. London* A350 (1976) 1–26.
21. A. Pearson, *Hydrodynamics of Jet Impact in a Collapsing Bubble.* PhD thesis, The University of Birmingham (2002) 223 pp.
22. T.B. Benjamin and A.T. Ellis, The collapse of cavitation bubbles and the pressures thereby produced against solid boundaries. *Phil. Trans. R. Soc. London* A260 (1966) 221–240.
23. J.R. Blake, The Kelvin impulse: Application to cavitation bubble dynamics. *J. Austral. Math. Soc.* B30 (1988) 127–146.
24. Y. Tomita and A. Shima, Mechanisms of impulsive pressure generation and damage pit formation by bubble collapse. *J. Fluid Mech.* 169 (1986) 535–564.